Journal of Materials Chemistry C

High performance UV-visible dual-band photodetector based on inorganic Cs_2SnI_6 perovskite/ZnO heterojunction structure

Journal:	*Journal of Materials Chemistry C*
Manuscript ID	TC-ART-10-2019-005940.R1
Article Type:	Paper
Date Submitted by the Author:	28-Nov-2019
Complete List of Authors:	Shao, Dali; Rensselaer Polytechnic Institute, Electrical, Computer, and Systems Engineering Zhu, Weiguang; Rensselaer Polytechnic Institute, Mechanical, Aerospace & Nuclear Engineering Xin, Guoqing; Rensselaer Polytechnic Institute, Department of Mechanical, Aerospace and Nuclear Engineering Liu, Xueqing; Rensselaer Polytechnic Institute, Department of Electrical, Computer, and Systems Engineering Wang, Tianmeng; Rensselaer Polytechnic Institute, Department of Chemical and Biological Engineering, Department of Electrical, Computer and Systems Engineering Shi, Sufei; Rensselaer Polytechnic Institute, Chemical and Biological Engineering, Department of Electrical, Computer and Systems Engineering Lian, Jie; Rensselaer Polytechnic Institute, Mechanical, Aerospace & Nuclear Engineering Sawyer, Shayla; Rensselaer Polytechnic Institute, Electrical, computer and system engineering

SCHOLARONE™
Manuscripts

ARTICLE

High performance UV-visible dual-band photodetector based on inorganic Cs_2SnI_6 perovskite/ZnO heterojunction structure

Received 00th January 20xx,
Accepted 00th January 20xx

DOI: 10.1039/x0xx00000x

Dali Shao,[a]* Weiguang Zhu,[b] Guoqing Xin,[b] Xueqing Liu,[a] Tianmeng Wang,[ac] Sufei Shi, [ac] Jie Lian,[b]* and Shayla Sawyer[a]*

Inorganic metal halide (IMH) perovskites have recently emerged as highly promising optoelectronic materials due to their excellent material properties including: tunable direct bandgap, long carrier diffusion length, high carrier mobility and outstanding environmental stabilities. However, the peroformance of photodetectors fabricated from IMH perovskites so far are still limited as compared to their counterparts based on organic-inorganic hybrid perovskites. In this work, we demonstrate a high performance ultraviolet-visible (UV-Vis) dual-band photodetector based on Cs_2SnI_6/ZnO heterojunction structure. By adjusting the polarity of the applied bias voltage, the photodetector can switch between two operation modes: (1) UV-Vis dual-band detection mode and (2) visible-blind UV detection mode. High detectivity in both UV (1.39×10^{12} jones) and visible (5.88×10^{11} jones) regions are achieved. In addition, this photodetector demonstrated a fast response speed with rise and fall time on the order of milliseconds and a large linear dynamic range of 119 dB. The excellent performance of this photodetector originates from efficient charge separation at the heterojunction interfaces, which will be discussed in detail in terms of the energy band diagrams and carrier dynamics of the device. Our study demonstrates the great application potential of inorganic vacancy-ordered perovskite in high-performance heterojunction photodetectors.

Introduction

Organic-inorganic hybrid perovskites have been considered to be promising for future optoelectronic applications due to many of their excellent material properties including tunable direct bandgap, large optical absorption coefficients, long carrier diffusion lengths, and high carrier mobility.[1-8] Indeed, significant progress have been achieved in organic-inorganic hybrid perovskite based optoelectronic including highly sensitive photodetectors, broadband tunable light-emitting diodes (LEDs), highly efficient solar cell with power conversion efficiencies exceeding than 20%, etc.[9-16] Nevertheless, the environmental instability of organic-inorganic hybrid perovskite is still the main concern for their practical applications. To overcome this hurdle, many all-inorganic halide perovskites have been developed as alternative materials.[17–28] Among these materials, tin (Sn) based perovskites $ASnX_3$ (X= I, Br, Cl) have attracted particular interest due to their nontoxicity and excellent optoelectronic properties.[26-28] However, $ASnX_3$ are very sensitive to the ambient atmosphere (oxygen, moisture, etc.) and easily oxidized from Sn^{2+} to Sn^{4+}. Therefore, exploration for air-stable alternatives has become an urgent need. Very recently, chemically stable Sn^{4+} based vacancy-ordered double perovskite materials such as $Cs_2SnI_xCl_{6-x}$ and $Cs_2SnCl_{6-x}Br_x$ have been demonstrated for energy harvesting, light emitting, and narrow band light detection applications.[29-31] Unfortunately, the sensitivity of photodetectors fabricated from $Cs_2SnCl_{6-x}Br_x$ single crystals are limited ($<10^{11}$ jones), and the detection range are restricted within the visible region. One possible approach for improving the performance of inorganic perovskite photodetectors is to combine the perovskite layer with other functional materials to form bilayer hetero-structures. For example, Tong *et al*. developed a sensitive, self-driven near infrared photodetector based on $CsBi_3I_{10}$ perovskite/silicon heterojunction structure, very recently Cs_2SnCl_6/GaN heterojunction photodetector has been demonstrated with excellent narrow-band sensitivity in the UV region.[32, 33] A major challenge in designing of a heterojunction photodetector is the need to improve the photoresponse of the device while at the same time maintaining a low dark current, which is critical for achieving a high detectivity. Among many of potential semiconductor materials for constructing heterojunction with perovskite, ZnO can be a promising candidate due to its excellent optical and electrical properties including wide direct band gap (3.37 eV), large exciton binding

[a] Department of Electrical, Computer, and Systems Engineering, Rensselaer Polytechnic Institute, Troy, NY 12180, USA
E-mail: shaodali828@gmail.com, sawyes@rpi.edu
[b] Department of Mechanical, Aerospace and Nuclear Engineering, Rensselaer Polytechnic Institute, Troy, NY 12180, USA
E-mail: lianj@rpi.edu
[c] Department of Chemical and Biological Engineering, Rensselaer Polytechnic Institute, Troy, NY 12180, USA
Electronic Supplementary Information (ESI) available: See DOI: 10.1039/x0xx00000x

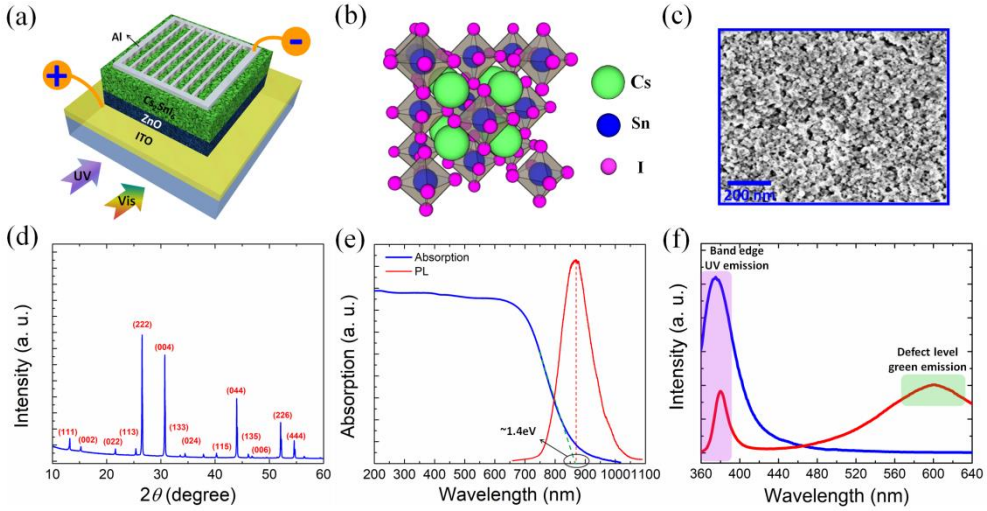

Fig. 1 (a) Schematic illustration of the Cs_2SnI_6/ZnO heterojunction photodiode. (b) Schematic illustration showing the crystal structure of the vacancy-ordered double perovskite Cs_2SnI_6. (c) SEM image of the Cs_2SnI_6 NPs thin film. (d) XRD pattern of the synthesized Cs_2SnI_6 NPs. (e) UV-Vis absorption spectrum and PL spectrum of the synthesized Cs_2SnI_6 NPs. (f) PL spectra of the ALD grown ZnO thin film before (red line) and after (blue line) hydrogen anneal.

energy (60 meV), high carrier mobility, and outstanding environmental stability. [34,35] In fact, for the same reason, ZnO has frequently been employed as an electron transfer layer in the fabrication of perovskite solar cells.[36-38] Among many different methods to grow ZnO thin films, atomic layer deposition (ALD) technique has great potential in fabrication of inorganic perovskites-based heterojunction photodetectors. ALD can provide thickness-controlled, dense and uniform thin films with minimum defects, which is critical to enhance the photocurrent and supress the dark current for heterojunction optoelectronic devices.[39-41] Remarkably, recent work done by G. Cen, *et al.* demonstrated a highly sensitive and stable $CsPbBr_3$ perovskite heterojunction photodetector by employing ALD as a powerful interfacial engineering technique for device performance tuning and optimization.[39]

In this work, we demonstrate a high performance UV-Vis dual-band photodetector based on Cs_2SnI_6/ZnO heterojunction structure. By adjusting the polarity of the applied bias voltage, the photodetector can switch between two operation modes: (1) UV-Vis dual-band detection mode and (2) visible-blind UV detection mode. Such unique function of this photodetector greatly extends its practical applications. Benefit from the excellent carrier separation efficiency at the hetero-interface, the device achieved high detectivity in both UV (1.39×10^{12} jones) and visible (5.88×10^{11} jones) regions. Furthermore, the photodetector demonstrated a fast response speed with rise and fall time on the order of milliseconds and a large linear dynamic range of 119 dB. The results in this work demonstrate the great application potential of inorganic vacancy-ordered perovskite in high performance heterojunction photodetectors. Further research toward this direction is highly desirable.

Results and discussion

Fig. 1a shows the three-dimensional schematic illustration of the Cs_2SnI_6/ZnO heterojunction photodiode. The crystal structure of the vacancy-ordered double perovskite Cs_2SnI_6 is illustrated in Fig. 1b, which represent a vacancy-ordered double perovskite structure with isolated [SnI_6] octahedral. The scanning electron microscope (SEM) image of the synthesized Cs_2SnI_6 NPs thin film is shown in Fig. 1c, the average size of the Cs_2SnI_6 NPs is estimated to be 20-30nm. XRD was performed on the sample to check for the crystallinity, as shown in Fig. 1d. The major peaks at the 2θ values: 13.2°, 15.2°, 21.6°, 25.4°, 26.6°, 30.8°, 44.1°, 52.0°, 54.6°, correspond to the atomic planes of (111), (002), (022), (113), (222), (004), (044), (226), (444), respectively. The room temperature UV-Vis absorption spectrum and photoluminescence (PL) spectrum of the Cs_2SnI_6 NPs are presented in Fig. 1e. The absorption spectrum shows a cut off wavelength at 860nm, corresponding to an optical band gap of ~1.4 eV. This optical band gap was further verified by PL spectroscopy. As shown in Fig. 1e, the PL spectrum excited at 520 nm pronounced PL peak ranging from 770 to 1000 nm with the peak centered at 861 nm, confirmed the effective optical band gap of ~1.4 eV of the synthesized Cs_2SnI_6 NPs. This is consistent with previous literature reports, where the bandgap values vary from 1.26 to 1.6 eV.[42-44] It is worth mentioning that the post growth hydrogen annealing treatment of the ALD grown ZnO thin film can greatly improve the film conductivity due to the introduction of shallow donor states such as the VO-H complex and the hydrogen interstitial

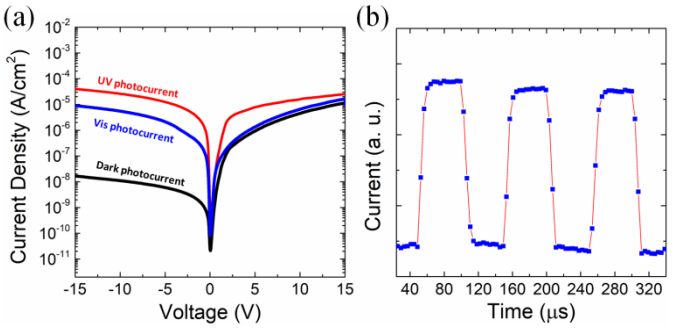

Fig. 2 (a) I-V characteristics of the photodetector measured in the dark, under 760 nm visible illumination, and 375 nm UV illumination. (b) Transient response of the heterojunction photodiode with a rising time of 4.3 μs and falling time of 5.2 μs measured under ambient conditions.

This journal is © The Royal Society of Chemistry 20xx

Please do not adjust margins

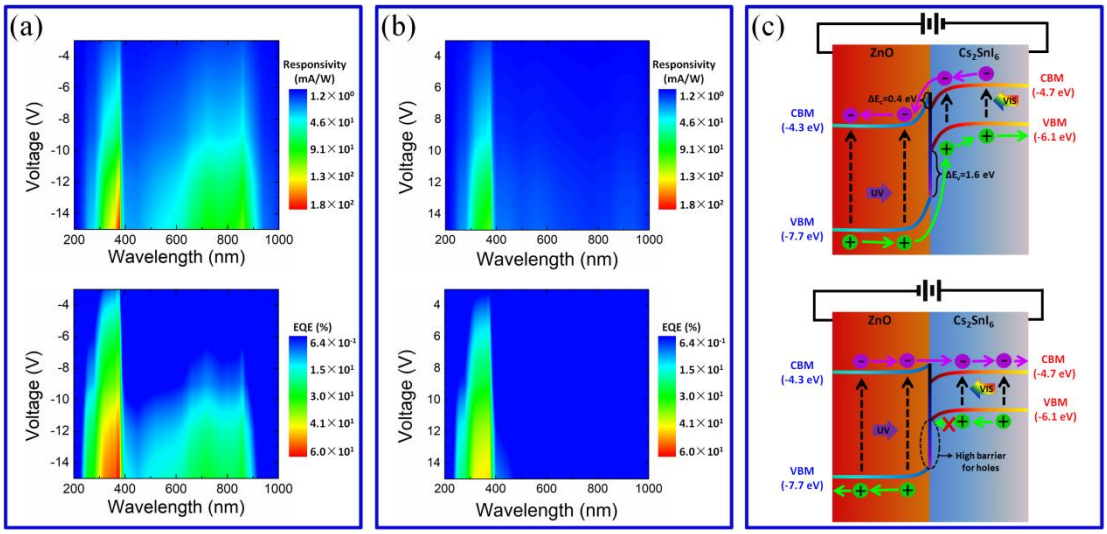

Fig. 3 (a) Photoresponsivity (top) and EQE (bottom) pseudo-color maps of this heterojunction photodiode measured under reverse bias voltages. (b) Photoresponsivity (top) and EQE (bottom) pseudo-color maps of this heterojunction photodiode measured under forward bias voltages. (c) Schematic energy band diagram showing the band alignment and carrier dynamics of this device operating under reverse bias (top) and forward bias (bottom) conditions.

.[45-47] In addition, the passivation effect of the post growth hydrogen annealing treatment can effectively cure the deep level defect and reduce the number of carrier scattering centers in the ZnO thin film, leading to improved electron mobility.[48] As demonstrated in Fig. 1f, the photoluminescence spectrum of the ZnO thin film after the hydrogen annealing treatment shows greatly enhanced band-edge UV emission centered at ~375 nm and suppressed defect level green emission centered at ~600 nm.

The I-V characteristics of the photodetector are measured in the dark, under 760 nm visible illumination, and under 375nm UV illumination, as shown in Fig. 2a. The dark current of the heterojunction photodiode shows an excellent rectifying characteristic with a high rectification ratio of 161 when biased at ±5V. When forward biased, the dark current increases exponentially following the equation $I \sim \exp(\alpha V)$. The constant α is calculated to be 0.34 V^{-1} by fitting the experimental data. Under reverse bias, the photocurrent generated by 760 nm visible/375 nm UV illumination are more than 500 times/three orders of magnitude higher than the dark current, demonstrating good signal to noise ratio of this device in both UV and visible region. Under forward bias, however the photocurrent generated by 375 nm UV light is less than two orders of magnitude higher than the dark current, and the photocurrent generated by 760 nm visible light is almost comparable to the dark current, suggesting a completely quench of photoresponse in the visible region. Such kind of voltage polarity dependent photosensitivity will be discussed in details later in this paper. The transient photoresponse of this device was measured under a 375 nm short pulse light from a LED, as presented in Fig. 3f. The rise time (output signal changing from 10% to 90% of the peak output value) and the decay time (output signal changing from 90% to 10% of the peak output value) of the photocurrent are 4.3 μs and 5.2 μs, respectively. This is faster than most of perovskite based photodetectors reported so far, indicating a good quality of the ZnO thin film and the Cs_2SnI_6 NPs.

Photoresponsivity is an important figure-of-merit for photodetectors, which is defined as photocurrent per unit of incident optical power. The photoresponsivity and EQE pseudo-color maps of this heterojunction photodiode measured under reverse bias and under forward bias are presented in Fig. 3a and Fig. 3b, respectively. As shown in Fig. 3a, the photoresponsivity and EQE pseudo-color map of this device under reverse bias shows two major detection bands. The first detection band is contributed by ZnO layer and is located in the UV region from 280 nm to 385 nm. A maximum photoresponsivity of 183.4 mA/W was measured at 378 nm wavelength, corresponding to an EQE of 60.2%. The second detection band located in visible region from ~ 600 - 900 nm is mainly contributed by Cs_2SnI_6 layer. A maximum responsivity of 113.4 mA/W was measured at 858 nm (1.44eV) wavelength, which agrees well with the bandgap of Cs_2SnI_6 (1.4eV) measured in this work. Under forward bias, however, only the UV detection band remains while the visible detection band completely quenched, as shown in Fig. 3b. A maximum responsivity of 108 mA/W at 374 nm was measured under forward bias, lower than that of measured at reverse bias condition. To understand this voltage polarity dependent photoresponse, we can refer to the schematic energy band diagram of this heterojunction shown in Fig. 3c. Based on the Anderson's model, the Cs_2SnI_6/ZnO heterojunction has a small conduction band offset of 0.4 eV and a large valance band offset of 1.6 eV. Since ZnO is highly transparent to visible light, most of the visible light can get through ZnO and be absorbed in the Cs_2SnI_6 film to generate electron-hole pairs (EHP). Under reversed bias conditions, the photogenerated electrons at the Cs_2SnI_6 side can transport through the interfacial barrier easily (due to the small conduction band offset) and drift toward the contact at the ZnO thin film side driven by the external electrical field. At the same time, the photogenerated holes in both ZnO and Cs_2SnI_6 drift toward the contact at the Cs_2SnI_6 side without any energy barriers.

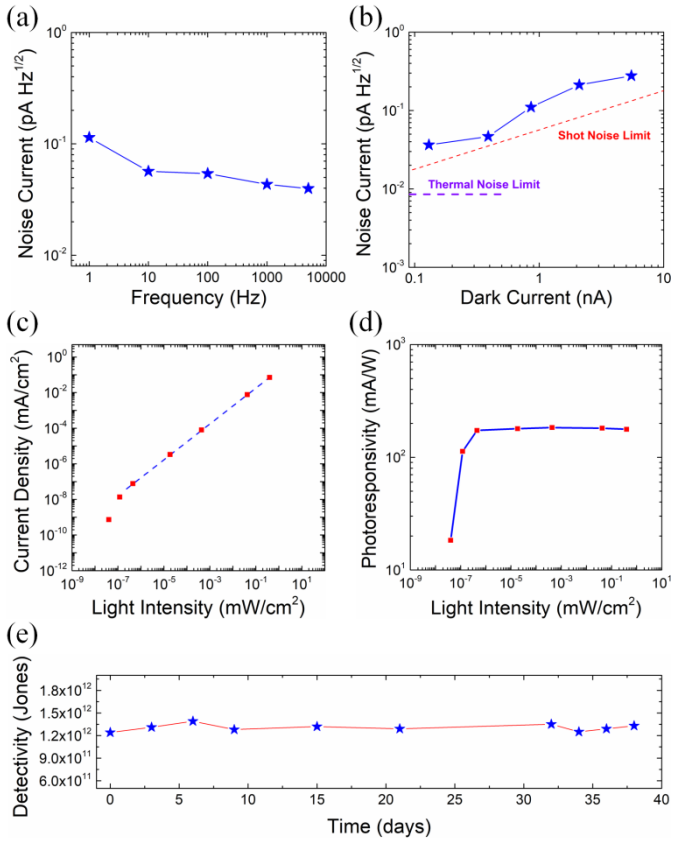

Fig. 4 (a) Noise current measured at various frequencies in the range from 1 Hz to 5K Hz. (b) Noise current measured at different dark current levels. (c) Photocurrent density measured at varying light intensity. (d) The consistency of the photoresponsivity measured over a wide range of light intensity. (e) The detectivity of the photodetector measured over time.

Therefore, the photogenerated electrons and holes in both ZnO and Cs_2SnI_6 can be collected to form the photocurrent signal, resulting UV-Vis dual detection band. To the contrary, when the heterojunction is forward biased, the photogenerated holes in the Cs_2SnI_6 side tend to drift toward the ZnO region under external electrical field but they cannot get through the interfacial region due to the high energy barrier (1.6 eV) there for holes. Therefore, without efficient charge separation at the hetero-interface under forward bias, the photogenerated holes in the Cs_2SnI_6 quickly recombine with the photogenerated electrons, leading to significant quench of the photoresponse in the visible band. Therefore, by adjusting the polarity of external bias, our device can operate in either UV-Vis dual detection band mode or visible-blind UV detection mode. This function greatly extend the photodetector's practical applications including secure space-to-space communications, pollution monitoring, water sterilization, flame sensing, early missile plume detection, security surveillance, etc.

Detectivity (D^*) is an important parameter that indicates the ability of a photodetector to measure weak optical signals. The D^* is expressed as:[49,50]

$$D^* = \frac{\sqrt{AB}}{NEP}$$

where the NEP = i_n/R is the noise equivalent power, A is the area of the device, B is the bandwidth, i_n is the measured noise current, and R is the photoresponsivity of the photodetector. The total noise current of the photodetector measured at various frequencies (range from 1 Hz to 5 kHz) and at different dark current levels are presented in Fig. 4a and Fig. 4b, respectively. As shown in Fig. 4a, the device show small noise current below 1.5×10^{-1} pA Hz$^{-1/2}$ and slowly decrease to 4×10^{-2} pA Hz$^{-1/2}$ at the frequency of 5000 Hz, indicating that 1/f noise of the device is the not main contributor to the total noise current. Generally, shot noise or thermal noise dominates the total noise in perovskite photodetectors. The shot noise $i_{n,s}$ can be expressed as:

$$i_{n,s} = \sqrt{2ei_dB}$$

where e is the element charge and i_d is the dark current of the device, and the thermal noise $i_{n,t}$ can be expressed as:

$$i_{n,t} = \sqrt{(4k_BTB)/R}$$

where k_B is the Boltzmann constant, T is the temperature, and R is the resistance of the device. The shot noise limit and thermal noise limit of this device is plotted in Fig. 4b. Clearly, the total noise of this device is mainly dominated by the shot noise. In the UV region, a maximum specific detectivity of 1.39×10^{12} jones was achieved at 378 nm, and in the visible region a maximum detectivity of 5.88×10^{11} jones was measured at 858 nm, demonstrating excellent sensitivity of this heterojunction photodetector in both UV and visible region. It is worth mentioning that the performance of the photodetector could be further improved through optimization of the Cs_2SnI_6 and ZnO layers thickness, which impacts the carrier recombination rate, carrier collection efficiency, and response speed of the photodetector.

In addition to the high detectivity, a constant responsivity from strong light all the way down to weak light is important for a detector so that it can be applied for weak light sensing. Every photodetector has a finite range of linear response and is characterized by linear dynamic range, in which the responsivity keeps constant. LDR is expressed as:[49,50]

$$LDR = 20\log(\frac{P_{high}}{P_{low}})$$

where P_{high} and P_{low} are the upper and lower limit of the incident light intensities that beyond this range the photocurrent begins to deviate from linearity. The LDR of the heterojunction photodiode was characterized by measuring the photocurrent at a fixed frequency of 10 Hz under 375 nm UV illumination with varying light intensity from 4×10^{-8} mW/cm^2 to 4×10^{-1} mW/cm^2, as shown in Fig. 4c. The photodetector demonstrated a linear photoresponse within the light intensity range from 4.5×10^{-7} mW/cm^2 to 4×10^{-1} mW/cm^2, corresponding to a LDR of 119 dB. Noted that this is comparable to Si photodetectors and are better than other types of photodetectors such as GaN (50 dB) and InGaAs (66 dB).[51] Fig. 4d is the photoresponsivity measured within above light intensity range, which shows a good consistency of the responsivity with light intensity range from 4.5×10^{-7} mW/cm^2 to 4×10^{-1} mW/cm^2. The detectivity of the photodetector over time is shown in Fig. 4e, no obvious detectivity degradation observed for more than 35 days after storage in 45% relative humidity conditions.

This journal is © The Royal Society of Chemistry 20xx

Please do not adjust margins

Table 1 Performance comparison of inorganic perovskite heterojunction photodetectors in previous literatures.

Device Structure	Measurement Wavelength [nm]	Maximum Responsivity [mA/W]	Rise/decay time [μs]	Detectivity [Jones]	LDR [dB]	References
$SnO_2/CsPbBr_3$	300	380	N/A	2.6×10^{11}	N/A	52
Cs_2SnCl_6/GaN	378	208	0.75/0.91	1.2×10^{12}	71	33
$CsPbBr_3/ZnO$	450	4250	210/240	N/A	N/A	36
$CsBi_3I_{10}$/Silicon	808	492.1	73/76	1.38×10^{11}	N/A	32
$CsPbBr_3$/InGaZnO	365	3794	2000/2000	NA	N/A	53
$Al_2O_3/CsPbBr_3/TiO_2$	405	440	28/270	1.88×10^{13}	~173	39
Cs_2SnI_6/ZnO	378	183.4	4.3/5.2	1.39×10^{12}	119	This Work

Conclusions

In conclusion, we demonstrated a Cs_2SnI_6/ZnO heterojunction photodetector with high performance UV-Vis dual-band sensing capability. The photodetector can switch between UV-Vis dual-band detection mode and visible-blind UV detection mode by adjusting the polarity of external bias. This unique function of this photodetector greatly extends its practical applications. Benefit from the excellent carrier separation efficiency at the hetero-interface, the device achieved high detectivity in both UV (1.39×10^{12} jones) and visible (5.88×10^{11} jones) regions under reverse bias. Furthermore, the photodetector demonstrated a fast response speed with rise and fall time on the order of microseconds and a large linear dynamic range of 119 dB. The results in this work can be of particular interest for future development of inorganic vacancy-ordered perovskite based high performance heterojunction photodetectors.

Experimental section

Growth of ZnO thin film

A ZnO thin film was grown on ITO substrate through atomic layer deposition (ALD) method (PICOSUN™ R-200 Advanced ALD system) with alternating diethylzinc and H_2O exposures:

(A) $ZnOH^* + Zn(CH_2CH_3)_2 \rightarrow ZnOZn(CH_2CH_3)^* + CH_3CH_3$

(B) $Zn(CH_2CH_3)^* + H_2O \rightarrow ZnOH^* + CH_3CH_3$

where the asterisks represent the surface species. By repeating these reactions in an ABAB... sequence, ZnO layer can be deposited with atomic layer control. The ZnO ALD reaction sequence was: i) dose diethylzinc to 1.0 Torr for 120 seconds; ii) evacuate reaction products and excess diethylzinc; iii) dose N_2 to 20.0 Torr for 60 seconds and then evacuate N_2 (repeat 5 times); iv) dose H_2O to 1.0 Torr for 120 seconds, v) evacuate reaction products and excess H_2O; vi) dose N_2 to 20.0 Torr for 60 seconds and then evacuate N_2 (repeat 5 times). This sequence constitutes one AB cycle of ZnO ALD. The ZnO ALD was performed at 150°C with 500 cycles and the thickness of the ZnO thin film is around 100nm. Finally, the ITO substrate with an ALD grown ZnO thin film is placed in a furnace for post-annealing treatment in Ar/H_2 (ratio, 96:4) atmosphere at 400 °C for 2 hours.

Synthesis of Perovskite NPs

Synthesis of Cs_2SnI_6 nanoparticles was using a reverse injection process based on metal ion metathesis. First 0.125 g SnI4 was dissolved in dried octadecene (ODE) at 60 °C. Cs-precursor was prepared by dissolving 0.082 g of Cs_2CO_3 in 0.5 mL of OLAH, 5 mL ODE, and 0.5 mL of OLAM by heating at 130 °C for 1.5 h. Then the Cs-precursor was heated to 200 °C under vigorous stirring followed by injection of SnI_4 solution. The colour of reaction immediately changed to brown. Reaction was continued for 1 hour and quenched by adding the product into dichlorobenzene. Then brown precipitation (Cs_2SnI_6 NPs) was washed by dichlorobenzene in a centrifuge at 3500 RPM for 20 min twice followed by drying in an oven at 60 °C overnight.

Fabrication of Cs_2SnI_6/ZnO heterojunction photodetector

For the device fabrication, the Cs_2SnI_6 NPs were dispersed in dichlorobenzene solvent and spin coated to the top of the ZnO thin film grown on ITO substrate at a speed of 3000 rpm for three times. The thickness of the Cs_2SnI_6 NPs thin film is ~300nm. Then Al contact with thickness of ~200 nm was deposited on the top of the device using e-beam evaporator. Finally, the photodetector was packaged and wire bonded using Epo-Tek H20E conductive epoxy. The effective device area is 0.16 cm^2 defined by the showdown mask.

Material and device characterization

The SEM images of the Cs_2SnI_6 NPs were taken using a Carl Zeiss Ultra 1540 dual beam SEM. The XRD patterns of the Cs_2SnI_6 NPs were measured using Bruker D8-Discover X-ray diffractometer. The UV-visible absorption spectrum of the Cs_2SnI_6 NPs was measured using Shimadzu UV-Vis 2550

spectrophotometer. The PL spectrum of Cs_2SnI_6 NPs was measured using on a home-built system with a continuous wave diode laser (532 nm) and a Si photodetector. The PL spectrum of the ZnO thin film was measured using a Spex-Fluorolog-Tau-3 spectrofluorometer with excitation wavelength fixed at 330 nm, respectively. The I-V characteristics of the Cs_2SnI_6/ZnO heterojunction photodetector were measured using a HP4155B semiconductor parameter analyser and LEDs with center peak wavelength at 760nm and 375 nm, respectively. The photoresponsivity and EQE pseudo-color maps of the device as a function of bias voltages were measured using a Shimadzu UV-Vis 2550 spectrophotometer in connection with a commercial optical power meter. The total noise current of the photodetector at room temperature was directly measured with an SR830 lock-in amplifier at different dark current levels and at various frequencies (range from 1 Hz to 5 kHz).

Conflicts of interest

The authors declare no conflict of interest.

Acknowledgements

Prof. Sawyer and Dr. Shao acknowledge funding support from New Knowledge and Innovation Program (KIP) Seed Grant program at Rensselaer Polytechnic Institute. Prof. Lian acknowledges the support from the Center for Performance and Design of Nuclear Waste Forms and Containers, an Energy Frontier Research Center funded by the U.S. Department of Energy, Office of Science, Basic Energy Sciences under Award # DE-SC0016584.

Notes and references

1 S. D. Stranks, G. E. Eperon, G. Grancini, C. Menelaou, M. J. P. Alcocer, T. Leijtens, L. M. Herz, A. Petrozza and H. J. Snaith, *Science*, 2013, **342**, 341-344.
2 G. C. Xing, N. Mathews, S. Y. Sun, S. S. Lim, Y. M. Lam, M. Gra ̈tzel, S. Mhaisalkar and T. C. Sum, *Science*, 2013, **342**, 344-347.
3 J. Miao and F. Zhang, *J. Mater. Chem. C*, 2019, **7**, 1741-1791.
4 Y. Dong, Y. Zou, J. Song, X. Song and H. Zeng, *J. Mater. Chem. C*, 2017, **5**, 11369-11394.
5 J. Albero and H. Garcá, *J. Mater. Chem. C*, 2017, **5**, 4098-4110.
6 L. Qiu, J. Deng, X. Lu, Z. Yang and H. Peng, *Angew. Chem. Int. Ed.*, 2014, **53**, 1-5.
7 I. E. Rauda, R. Senter and S. H. Tolbert, *J. Mater. Chem. C*, 2013, **1**, 1423-1427.
8 C. Han, H. Yu, J. Duan, K. Lu, J. Zhang, M. Shao and B. Hu, *J. Mater. Chem. C*, 2018, **6**, 6164-6171.
9 X. Hu, X. Zhang, L. Liang, J. Bao, S. Li, W. Yang and Y. Xie, *Adv. Funct. Mater.*, 2014, **24**, 7373-7380.
10 Z.-K. Tan, R. S. Moghaddam, M. L. Lai, P. Docampo, R. Higler, F. Deschler, M. Price, A. Sadhanala, L. M. Pazos, D. Credgington, F. Hanusch, T. Bein, H. J. Snaith and R. H. Friend, *Nat. Nanotechnol.*, 2014, **9**, 687-692.
11 G. Li, Z.-K. Tan, D. Di, M. L. Lai, L. Jiang, J. H.-W. Lim, R. H. Friend and N. C. Greenham, *Nano Lett.*, 2015, **15**, 2640-2644.
12 L. Dou, Y. Yang, J. You, Z. Hong, W.-H. Chang, G. Li and Y. Yang, *Nat. Commun.*, 2014, **5**, 5404.
13 M. I. Saidaminov, V. Adinolfi, R. Comin, A. L. Abdelhady, W. Peng, I. Dursun, M. Yuan, S. Hoogland, E. H. Sargent and O. M. Bakr, *Nat. Commun.*, 2015, **6**, 8724.
14 Y. Fang, Q. Dong, Y. Shao, Y. Yuan and J. Huang, *Nat. Photonics* 2015, **9**, 679-686.
15 W. S. Yang, J. H. Noh, N. J. Jeon, Y. C. Kim, S. Ryu, J. Seo and S. I. Seok, *Science*, 2015, **348**, 1234-1237.
16 N. Arora, M. I. Dar, A. Hinderhofer, N. Pellet, F. Schreiber, S. M. Zakeeruddin, M. Grätzel, *Science*, 2017, **358**, 768-771.
17 H. Chen, A. Guo, J. Zhu, L. Cheng and Q. Wang, *Appl. Surf. Sci.*, 2019, **465**, 656-664.
18 L. Xu, Y. Wan, H. Xie, Y. Huang, L. Yang, L. Qin and H. J. Seo, *Appl. Surf. Sci.*, 2016, **389**, 849-857.
19 M. Kulbak, D. Cahen and G. Hodes, *J. Phys. Chem. Lett.*, 2015, **6**, 2452-2456.
20 A. Swarnkar, A. R. Marshall, E. M. Sanehira, B. D. Chernomordik, D. T. Moore, J. A. Christians, T. Chakrabarti and J. M. Luther, *Science*, 2016, **354**, 92-95.
21 L. Protesescu, S. Yakunin, M. I. Bodnarchuk, F. Krieg, R. Caputo, C. H. Hendon, R. X. Yang, A. Walsh and M. V. Kovalenko, *Nano Lett.*, 2015, **15**, 3692-3696.
22 J. Song, J. Li, X. Li, L. Xu, Y. Dong and H. Zeng, *Adv. Mater.*, 2015, **27**, 7162-7167.
23 X. Zhang, B. Xu, J. Zhang, Y. Gao, Y. Zheng, K. Wang and X. W. Sun, *Adv. Funct. Mater.*, 2016, **26**, 4595-4600.
24 X. Li, Y. Wu, S. Zhang, B. Cai, Y. Gu, J. Song and H. Zeng, *Adv. Funct. Mater.*, 2016, **26**, 2435-2445.
25 J. Duan, H. Xu, W. E. I. Sha, Y. Zhao, Y. Wang, X. Yang amd Q. Tang, *J. Mater. Chem. C*, 2019, **7**, 21036-21068.
26 G. Nasti and A. Abate, *Adv. Energy Mater.*, 2019, 1902467.
27 N. K. Noel, S. D. Stranks, A. Abate, C. Wehrenfennig, S. Guarnera, A. Haghighirad, A. Sadhanala, G. E. Eperon, S. K. Pathak, M. B. Johnston, A. Petrozza, L. M. Herz and H. J. Snaith, *Energy Environ. Sci.*, 2014, **7**, 3061-3068.
28 F. Hao, C. C. Stoumpos, D. H. Cao, R. P. H. Chang, M. G. Kanatzidis, *Nat. Photon.*, 2014, **8**, 489-494.
29 B. Lee, C. C. Stoumpos, N. Zhou, F. Hao, C. Malliakas, C.-Y. Yeh, T. J. Marks, M. G. Kanatzidis and R. P. H. Chang, J. *Am. Chem. Soc.*, 2014, **136**, 15379-15385.
30 J. Zhou, J. Luo, X. Rong, P. Wei, M. S. Molokeev, Y. Huang, J. Zhao, Q. Liu, X. Zhang J. Tang and Z. Xia, *Adv. Optical Mater.*, 2019, **7**, 1900139.
31 Z. Tan, J. Li, C. Zhang, Z. Li, Q. Hu, Z. Xiao, T. Kamiya, H. Hosono, G. Niu, E. Lifshitz, Y. Cheng and J. Tang, *Adv. Funct. Mater.*, 2018, **28**, 1801131.
32 X.-W. Tong, Z.-X. Zhang, D. Wang, L.-B. Luo, C. Xie and Y.-C. Wu, *J. Mater. Chem. C*, 2019, **7**, 863-870.
33 D. Shao, W. Zhu, G. Xing, J. Lian and S. Sawyer, *Appl. Phys. Lett.*, 2019, **115**, 121106.
34 C.-Y. Chang, F.-C. Tsao, C.-J. Pan, G.-C. Chi, H.-T. Wang, J.-J. Chen, F. Ren, D. P. Norton, S.J. Pearton, K.-H. Chen and L.-C. Chen, *Appl. Phys. Lett.*, 2006, **88**, 173503.
35 D. C. Look, C. Coskun, B. Claflin and G. C. Farlow, Physica B, 2003, **340**, 32-38.
36 H. Liu, X. Zhang, L. Zhang, Z. Yin, D. Wang, J. Meng, Q. Jiang, Y. Wang and J. You, *J. Mater. Chem. C*, 2017, **5**, 6115-6122.
37 R. Zhang, C. Fei, B. Li, H. Fu, J. Tian and G. Cao, *ACS Appl. Mater. Interfaces*, 2017, **9**, 9785-9794.
38 D. Liu and T. L. Kelly, *Nat. Photonics*, 2014, **8**, 133–138.
39 G. Cen, Y. Liu, C. Zhao, G. Wang, Y. Fu, G. Yan, Y. Yuan, C. Su, Z. Zhao and W. Mai, *Small*, 2019, 15, 1902135.

 This journal is © The Royal Society of Chemistry 20xx

Please do not adjust margins

40 G. Yan, C. Zeng, Y. Yuan, G. Wang, G. Cen, L. Zeng, L. Zhang, Y. Fu, C. Zhao, R. Hong, and W. Mai, *ACS Appl. Mater. Interfaces*, 2019, 11, 32097-32107.

41 D. Shao, H. Sun, G. Xin, J. Lian, S. Sawyer, *Appl. Surf. Sci.* 2014, 314, 872-876.

42 B. Lee, C. C. Stoumpos, N. Zhou, F. Hao, C. Malliakas, C.-Y. Yeh, T. J. Marks, M. G. Kanatzidis and R. P. H. Chang, *J. Am. Chem. Soc.*, 2014, **136**, 15379-15385.

43 X. Qiu, B. Cao, S. Yuan, X. Chen, Z. Qiu, Y. Jiang, Q. Ye, H. Wang, H. Zeng, J. Liu amd M. G. Kanatzidis, *Solar Energ. Mater. Solar Cells*, 2017, **159**, 227-234.

44 B. Saparov, J.-P. Sun, W. Meng, Z. Xiao, H.-S. Duan, O. Gunawan, D. Shin, I. G. Hill, Y. Yan and D. B. Mitzi, *Chem. Mater.*, 2016, **28**, 2315-2322.

45 D. Shao, M. Yu, J. Lian and S. Sawyer, *Appl. Phys. Lett.*, 2012, **101**, 211103.

46 A. Janotti and C. G. Van de Walle, *Nat. Mater.*, 2007, **6**, 44-47.

47 P. F. Cai, J. B. You, X. W. Zhang, J. J. Dong, X. L. Yang, Z. G. Yin and N. F. Chen, *J. Appl. Phys.*, 2009, **105**, 083713.

48 J. B. Varley, H. Peelaers, A. Janotti and C. G. Van de Walle, *J. Phys. Condens. Mat.*, 2011, **23**, 334212.

49 C. Bao, Z. Chen, Y. Fang, H. Wei, Y. Deng, X. Xiao, L. Li and J. Huang, *Adv. Mater.*, 2017, 29, 1703209.

50 Z. Yang, M. Le, M. Wang, K. Zhang, X. Li, J. Shao and W. Chen, *IEEE Sens. J.*, 2017, **17**, 4447-4453.

51 X. Gong, M. Tong, Y. Xia, W. Cai, J. S. Moon, Y. Cao, G. Yu, C. L. Shieh, B. Nilsson and A. J. Heeger, *Science*, 2009, **325**, 1665−1667.

52 Y. Zhang, W. Xu, X. Xu, J. Cai, W. Yang and X. Fang, *J. Phys. Chem. Lett.* 2019, 10, 836-841.

53 M. Sun, Q. Fang, Z. Zhang, D. Xie, Y. Sun, J. Xu, W. Li, T. Ren and Y. Zhang, *ACS Appl. Mater. Interfaces*, 2018, 10, 8, 7231-7238.

This journal is © The Royal Society of Chemistry 20xx

Please do not adjust margins

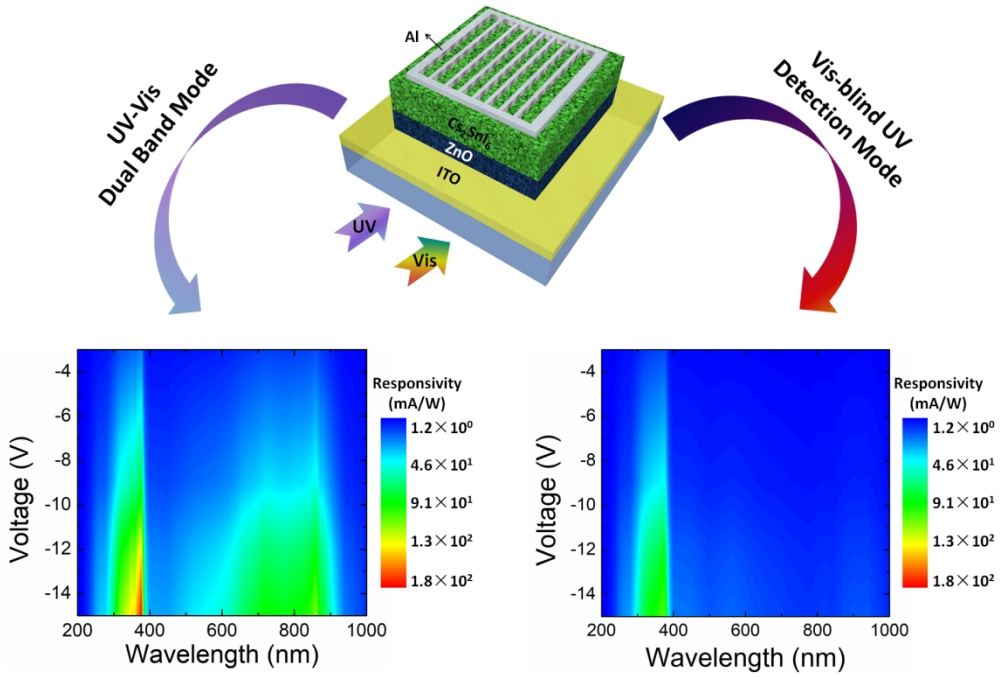

397x270mm (120 x 120 DPI)